NUMERICAL STUDY OF SEPARATED FLOW IN A PLANE ASYMMETRIC DIFFUSER

Johan Gullman-Strand, Gustav Amberg and Arne V. Johansson
Department of Mechanics, KTH
SE-100 44 Stockholm, Sweden

ABSTRACT

Computations of the turbulent flow through plane asymmetric diffusers (PAD) for opening angles from 8° to 10° have been carried out. The fractional step finite element formulation of Guermond and Quartapelle (1997) for the Reynolds Averaged Navier-Stokes (RANS) equations has been combined with the non-linear Explicit Algebraic Reynolds Stress Model (EARSM) of Wallin and Johansson (2000) and the Wilcox (1993) low Re K-ω formulation. The standard EARSM has been complemented with strain rate based streamline curvature correction (Wallin and Johansson, 2002). The computations are compared to experiments of Törnblom et al. (2002) for 8.5° and Buice and Eaton (2000) for the 10° PAD.

INTRODUCTION

The plane asymmetric diffuser (PAD) geometry is found in many industrial applications such as ventilation and jet engine inflow ducts. A large separation region forms on the inclined wall, extending into the outflow channel. Unlike the backward facing step the PAD does not have a predetermined separation point, which poses a great challenge on numerical simulations and turbulence modelling to accurately capture this phenomenon.

The case of 10° opening angle and Re_H= 20 000 has been studied previously in a number of investigations. Experimental results for the 10° case have been reported by Obi et al. (1993) and Buice and Eaton (2000), LES-calculations performed by Kaltenbach et al. (1999) and an ERCOFTAC workshop, (Hellsten and Rautaheimo, 1999) was dedicated to this case. Apsley and Leschziner (2000) and Gullman-Strand et al., 2002 have earlier reported computations for that case.

The present work also presents computational results for the case with 8.5° opening angle, for which recent experimental data now are available (Törnblom et al., 2002). The experimental data provide a high degree of span-wise uniformity as well as good turbulence statistics, making them ideal as a test case for turbulence models and 2-D computational approaches.

Results for a PAD with 8° opening angle are presented to give a broadened picture of the PAD flow case. This is the smallest angle for which there is a separation bubble using the present numerical code. Computations have been performed for a 7.5° PAD but the flow was then found to be attached along the upper inclined wall throughout the diffuser.

The geometrical and flow parameters are the same as in the Törnblom et al. (2002) experiment with outlet/inlet channel height ratio H_{out}/H=4.7, opening angle varying from ϕ=8° to 10° and inlet Reynolds number Re_H=40 000. The corner radius at the beginning and end of the diffuser was $9.7H$. In accordance with the ERCOFTAC guidelines the turbulent inlet conditions were set ten inlet heights upstream of the diffuser. The diffuser lengths are listed in table 1

ϕ	8°	8.5°	10°
L_d	26.3	24.8	21.0

Table 1: Diffuser lengths depending on opening angle, normalized with inlet height.

MATHEMATICAL MODEL

Computations have been carried out with a RANS with EARSM formulation of the Reynolds stress tensor, both with and and without curvature correction together with low Reynolds number $K-\omega$ transport equations. The standard EARSM model will be denoted (WJ) and the curvature corrected (CC-WJ).

In the eddy-viscosity hypothesis the Reynolds stress tensor $\overline{u_i'u_j'}$ is modeled by a linear relation of the mean strain rate $S_{ij} = (U_{i,j} + U_{j,i})/2$ as

$$-\overline{u_i'u_j'} = 2\nu_T S_{ij} - \frac{2}{3}K\delta_{ij} \tag{1}$$

The implementation of the EARSM described by Wallin and Johansson (2000) was done by introducing the anisotropy tensor a_{ij} in the expression for the Reynolds stress as $\overline{u_i'u_j'} = K(a_{ij} + 2/3\delta_{ij})$. The expression for the 2D case treated here reduces to solving for (in boldface matrix notation) the explicit relation

$$\begin{aligned}\mathbf{a} = {} & f_1\beta_1\hat{\mathbf{S}} \\ & + (1-f_1^2)\frac{3B_2-4}{2\max(II_S, II_S^{eq})}\left(\hat{\mathbf{S}}^2 - \frac{1}{3}II_S\mathbf{I}\right) \\ & + \left(f_1^2\beta_4 - (1-f_1^2)\frac{B_2}{\max(II_S, II_S^{eq})}\right)(\hat{\mathbf{S}}\hat{\mathbf{\Omega}} - \hat{\mathbf{\Omega}}\hat{\mathbf{S}})\end{aligned} \tag{2}$$

with damping function f_1, coefficients $\beta_{1,4}$ and constants B_2 and II_S^{eq}. $\hat{\mathbf{S}}$ and $\hat{\mathbf{\Omega}}$ here represent the mean strain and rotation rate tensors, non-dimensionalized by the turbulence time scale τ. To compensate for streamline curvature a correction term to the mean rotation rate tensor was derived by Wallin and Johansson (2002). The mean rotation rate tensor is defined as $\hat{\Omega}_{ij}=\tau/2\,(U_{i,j} - U_{j,i})$. With curvature correction it reads

$$\hat{\Omega}_{ij}^{(*)} = \hat{\Omega}_{ij} - \frac{\tau}{A_0}\Omega_{ij}^{(r)} = \hat{\Omega}_{ij} + \frac{\tau}{A_0}\epsilon_{ijk}\omega_k^{(r)} \tag{3}$$

The strain rate based correction was derived by Wallin and Johansson (2002) and confirmed by the work of Hellsten et al. (2002), in 2D mean flow it is expressed as

$$\omega_3^{(S)} = \frac{S_{11}\dot{S}_{12} - S_{12}\dot{S}_{11}}{2S_{11}^2 + 2S_{12}^2} \tag{4}$$

with superscript (S) denoting the use of strain rate based curvature correction. Note that in equation (4) the $\hat{S}$ notation has been be dropped for simplicity and the dot represents the material derivative D/Dt. Wallin and Johansson (2002) also determined the value of the calibration constant, A_0=-0.72, which has been used in the present computations.

Modification of the turbulence time scale transport equation

Previously, one disadvantage of using the inverse of the turbulence time scale ω as complementary quantity to the kinetic energy, has been the difficulty to capture the singular behaviour close to solid walls. The rapid variation is described by

$$\omega \rightarrow \frac{6\nu}{\beta y^2} \quad \text{for} \quad y \leq 2.5\ \nu/u_\tau \tag{5}$$

The low-Re version of the transport equation for ω in the EARSM formulation is

$$\frac{\mathrm{D}\omega}{\mathrm{D}t} = \mathcal{P}_\omega - \beta\omega^2 + \nabla\left[(\nu + \sigma\nu_T)\,\nabla\omega\right] \tag{6}$$

with $\mathcal{P}_\omega$=$\alpha\omega a_{ij} S_{ij}$. For the destruction and diffusion terms, the singular behaviour becomes especially troublesome since the terms behave as y^{-4} as $y \rightarrow 0$ in near-wall shear flow. A decomposition is introduced as $\omega = \tilde{\omega} + \omega_{wall}$ with ω_{wall} given by equation (5) in the whole domain and $\tilde{\omega}|_{y=0} = 0$. The problem of computing the rapid growth of ω has now been transferred to handling the prescribed function ω_{wall}. The near wall diffusion and destruction terms associated with ω_{wall} cancel and equation (6) simplifies to

$$\begin{aligned}\frac{\mathrm{D}\tilde{\omega}}{\mathrm{D}t} &= \mathcal{P}_\omega - \beta(\tilde{\omega}^2 + 2\tilde{\omega}\omega_{wall}) \\ &\quad + \nabla\left[(\nu + \sigma\nu_T)\,\nabla\tilde{\omega}\right] + \nabla\left[\sigma\nu_T\nabla\omega\right]\end{aligned} \tag{7}$$

In the EARSM context two terms on the right hand side are still singular at the wall ($\sim y^{-1}$). The main balance in the immediate vicinity of the wall becomes 0=-$\alpha\omega_{wall} a_{ij} S_{ij}$ − $2\beta\tilde{\omega}\omega_{wall}$ from which we find that

$$\tilde{\omega}^+ \rightarrow -\frac{\alpha}{2\beta} a_{12} \quad \text{as} \quad y^+ \rightarrow 0 \tag{8}$$

in a plane turbulent channel flow (note that $a_{12} \sim y^+$ as $y^+ \rightarrow 0$) and hence the singular near wall behaviour has been eliminated when solving for $\tilde{\omega}$.

Wall normal distance function

In turbulence modelling, the need to introduce the wall normal distance in i.e. damping functions often arises. This is also needed in the above defined ω_{wall} as well as the EARSM damping function f_1. In order to obtain the wall normal distance at any point in the domain, independent of the complexity of the boundary shape, a distance function is computed, using ideas from level set methods (Sethian, 1996). By solving the evolution equation

$$\frac{\partial\phi}{\partial t} - (1 - |\nabla\phi|) = \mu_\phi \nabla^2\phi \tag{9}$$

for the scalar ϕ in the whole domain with the solid wall boundary condition $\phi_{wall} = 0$, ϕ will take the value of the shortest wall normal distance for each node in the domain. A diffusion term with μ_ϕ acting as a numerical viscosity, set proportional to the radius of the local element, is also introduced to damp noise and avoid swallow tail effects. This enables the introduction of wall normal distance dependent equations, without the need to formulate mesh or domain specific functions.

NUMERICAL MODEL

Introduction of automated code generation methodology in turbulence model development as well as practical engineering calculations drastically cuts down cycle time for the derivation of the numerical model and coding to a matter of minutes. It also presents the possibility to easily modify a generic set of governing equations for many types of flows.

Using the femLego toolbox (Amberg et al., 1999) together with Maple, the partial differential equations, the boundary conditions and initial conditions as well as the method of solving each equation is specified in a Maple worksheet and the FEM code is generated with the femLego toolbox from that sheet. Maple presents the equations in a readable and adjustable format and all documentation is contained within the script. It also gives the possibility to derive the equations in the language of applied mathematics. It is now possible to formulate the models in terms of applied mathematics and introduce parameter or easily change individual terms.

Once the code is generated and compiled, the mesh is created by a generic unstructured mesh generator.

The structured mesh consisted in all three cases of 318×75 nodes in the stream-wise and wall normal directions respectively, of which 120×75 were placed in the diffuser. The turbulence inlet conditions were obtained from channel flow calculations using the same computational code. The mesh was refined close to the wall with the first node placed at $0.35y^+$ in the inlet channel, increasing to $1.63y^+$ in the outlet channel. This was sufficient to resolve the near wall behaviour of the turbulence transport quantities in combination with the decomposition of the inverse turbulence time scale ω.

RESULTS

Computations have been made for opening angles from 7.5° to 10°, all with Reynolds number Re_H=40 000. Computations at 7.5° opening angle showed no separated region and will be left out in the following discussion. The smallest opening angle for which a separation bubble appeared on the inclined wall was 8° for both the WJ and CC-WJ models.

For the case of 8.5° opening angle, the numerical results have been compared to the experiments of Törnblom et al. (2002). The experimental results were obtained using a combination of PIV and LDV laser measurement techniques.

The experimental results of Buice and Eaton (2000) for 10° are used for comparison, but the reader should take note of the fact that the computations presented here are done with Re_H=40 000 while the experiments were done with Re_H=20 000.

Mean quantities and stream function

The extent of the separation bubble was determined using the dividing streamline (Ψ=0). The stream function Ψ is defined as

$$\Psi(x,y) = 1 - \frac{1}{U_b H}\int_0^y U(x,y)\,\mathrm{d}y \tag{10}$$

Results reported in Gullman-Strand et al. (2002) used U=0 as a measure of the extent of the separation, but the dividing streamline gives a more correct picture of the region with recirculating flow. Figure 1 shows the dividing streamlines for

the three opening angles. Generally the curvature corrected calculations show a substantially larger separation region both in streamwise and wall-normal direction. In the 8.5° case the curvature correction gives a result closer to the experimental one. The separation point moves up-stream and the reattachment point moves downstream as the angle is increased, see table 2. When increasing the opening angle the difference in prediction of separation point decrease between the WJ and CC-WJ models, while the difference in reattchment point grows. In the experiments of Törnblom et al. (2002) the backflow coefficient showed a larger spread in the position of the reattachment point than for the separation point. This is also underlined by the large difference of the reattachment point between the WJ and CC-WJ calculations.

The skin friction coefficient C_f can also be used as an indication of the streamwise extent of the separation bubble since it vanishes at the separation and reattachment points. Figure 2 shows the skin friction coefficient along the inclined wall of the diffuser at the three opening angles using the WJ model. The near wall resolution of the experimental values of U at 8.5° and 10° are too poor due to the use of optical measuring techiques and would rather require oil-film measurements. There is a large discrepancy in the separation point when comparing figures 1 and 2 due to the different resolutions. The skin friction coefficient is based on the wall normal velocity derivative $\partial U/\partial y$ at the wall and can be plotted as a function of x/H while Ψ is an integral quantity used in the whole domain. Table 2 lists the separation and attachment points for all angles, models and experiments. The magnitude of the back flow is underperdicted by the

		Separation point	Reattachment point
8°	WJ	15	27
	CC-WJ	12.5	29
8.5°	WJ	11	27
	CC-WJ	10	31
	Exp.	9	31
10°	WJ	4.5	28
	CC-WJ	5	32
	Exp	8	26

Table 2: Streamwise position x/H of separation and reattachment points for the three PADs

computations compared to the 8.5° PAD but overpredicted compared to the 10° experiments, as seen in figures 3 and 4. Curvature correction improves the behavior but is not a full remedy.

Reynolds stresses

The Reynolds shear stress distributions through the 8.5° PAD are shown in figure 5. The agreement between computations and experiments for componens $\overline{u'^2}$ and $\overline{w'^2}$ are very good in the entrance of the diffuser, but the computational results show a decrease in magnitude relative to the experiments. The velocity correlation $\overline{u'v'}$ shows good agreement through the whole diffuser. In figure 6 the $\overline{u'^2}$ distribution is compared for the three different opening angles. As expected the magnitude increases with opening angle but the difference in peak value near the inclined wall in the 10° case vanishes downstream.

The computational value of the turbulence kinetic energy $K = \overline{u_i'u_i'}/2$ for the 8.5° case is over-predicted in the

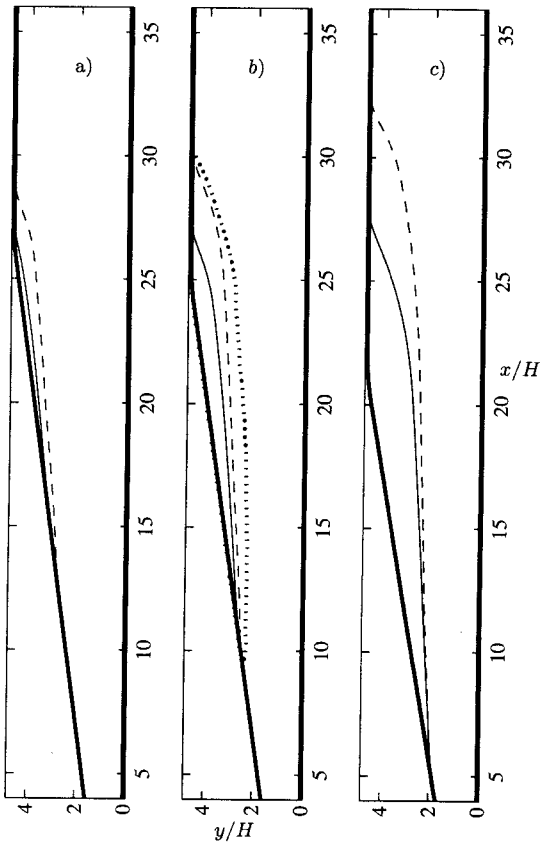

Figure 1: Dividing streamline for the cases a) 8.0°, b) 8.5° and c)10°. Solid lines show the standard WJ, dashed line CC-WJ and the experimental data of Törnblom et al. (2002) for 8.5° is shown as dotted line in figure b)

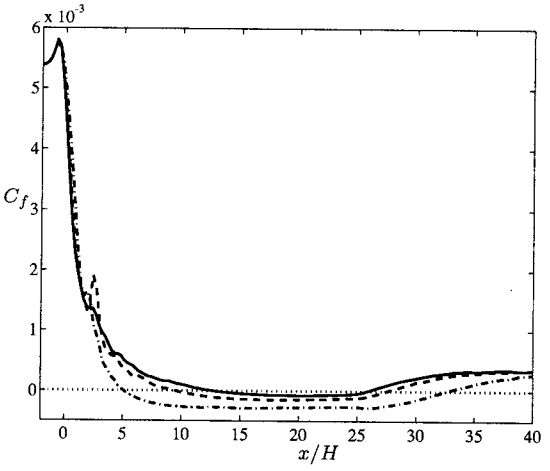

Figure 2: Skin friction coefficient along the inclined wall using the WJ model for 8°(—), 8.5°(- - -) and 10°(- · -).

beginning of the diffuser due to the high values of $\overline{v'^2}$ while it is under-predicted in the outlet channel influenced by the low values of $\overline{v'^2}$ in this region. However the production of kinetic energy, $\mathcal{P} = \overline{u_i'u_j'}\partial U_i/\partial x_j$ is in good agreement with experimental data downstream of $10x/H$, see figure 7. This shows that the destruction of K, here modelled as

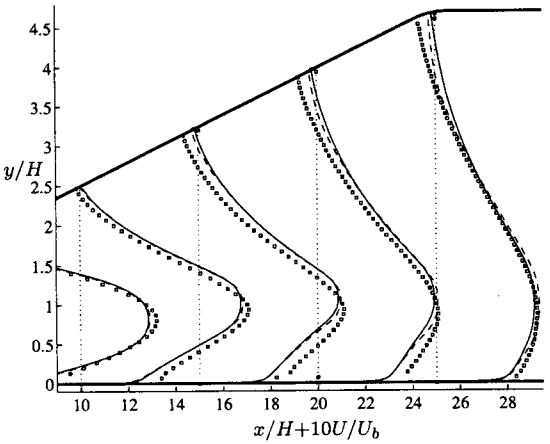

Figure 3: Close-up of the mean streamwise velocity for the 8.5° case with WJ (—), CC-WJ(- - -) and experiments (□).

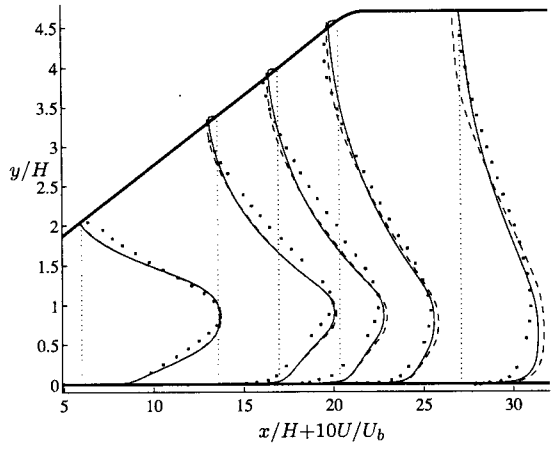

Figure 4: Mean streamwise velocity for the 10° case with WJ (—), CC-WJ(- - -) and experiments (□).

$\mathcal{P}_K = -\beta^* \omega K$, and consequently ω is over-estimated.

The effect of curvature correction is shown in figure 8, where the CC-WJ shows a higher value of Reynolds stress component $\overline{v'^2}$ than WJ close to the upper wall at $4x/H$, where the streamline curvature occurs and a decrease in peak value at the lower straight wall for the same x-position.

The same effect can be found when looking at the turbulence kinetic energy in the beginning of the diffuser. Figure 9 shows the normalised kinetic energy at positions $4x/H$ and $8x/H$ downstream of the diffuser for the 10° case. At $4x/H$ the curvature correction gives a higher turbulence kinetic energy peak near the inclined wall.

CONCLUDING REMARKS

The methodology of generating a FEM-based CFD code through extensive use of automated code generation was demonstrated to be a feasible and attractive approach for analysing the case of asymmetric diffuser flow for a set of different opening angles.

The EARSM predictions of the asymmetric diffuser flow are in reasonable overall agreement with experimental observations. The streamwise extent of the separation bubble can be seen as a key quantity to capture in the computations. It is reasonably well predicted, and the quality of the prediction is found to be improved by the inclusion of curvature correction in the EARSM. The wall-normal extent of the separation bubble is less well predicted, and in particular the strength of the back flow is severely underpredicted in comparison with experimental results for the 8.5° case.

Acknowledgements

The authors like to thank the Swedish Strategic Research Foundation and the IVS Research School for funding.

REFERENCES

Amberg, G., Törnhardt, R. and Winkler, C., 1999, "Finite elemet simulations using symbolic computing", *Mathematics and Computers in Simulation*, Vol. 44, pp. 275–274.

Apsley, D. D. and Leschziner, M. A., 2000, "Advanced turbulence modelling of separated flow in a diffuser", *Flow, Turbulence and Combustion*,Vol. 63,No. 1–4, pp. 81–112.

Buice, C. U. and Eaton, J. K., 2000, "Experimental Investigation of Flow Through an Asymmetric Plane Diffuser", *Journal of Fluids Engineering*, Vol. 122, pp. 433 – 435.

Guermond, J. L. and Quartapelle, L., 1997, "Calculation of Incompressible Vicous Flow by an Unconditionally Stable Projection FEM", *Journal of Computational Physics*, Vol. 132, No. CP965587, pp. 12–33.

Gullman-Strand, J., Amberg, G. and Johansson, A. V., 2002, "Study of separated flow in an asymmetric diffuser", *Proceedings 9th European Turbulence Conference*, Southampton, UK, pp. 643–646.

Hellsten, A. and Rautaheimo, P., 1999, "Proceedings 8th ERCOFTAC/IAHR/COST Workshop on Refined Turbulence Modelling", Helsinki University of Technology.

Hellsten, A., Wallin, S., and Laine, S., 2002, "Scrutinizing curvature corrections for algebraic Reynolds stress models", *32nd AIAA Fluid Dynamics Conference*, St. Louis, MO, USA, pp. 1–15.

Kaltenbach, H. J., Fatica, M., Mittal, R., Lund, T. S. and Moin, P., 1999, "Study of flow in a planar asymmetric diffuser using large-eddy simulation", *Journal of Fluid Mechanics*, Vol. 390, pp. 151–185.

Obi, S., Aoki, K. and Masuda, S., 1993, "Experimental and Computational Study of Separating Flow in an Asymmetric Planar Diffuser", *9th Symposium on Turbulent Shear Flows*, Kyoto, Japan, Vol. 305, pp. 1–4.

Sethian, J. A., 1996, "Level Set Methods and Fast Marching Methods", Cambridge University Press.

Törnblom, O., Lindgren, B. and Johansson, A. V. , 2002, "Measurements and control of the flow in a plane asymmetric diffuser", *Proceedings 9th European Turbulence Conference*, Southampton, UK, pp. 243–246.

Wallin, S. and Johansson, A. V., 2000, "An Explicit Algebraic Reynolds Stress Model for incompressible and compressible turbulent flows", *Journal of Fluid Mechanics*, Vol. 403, pp. 89–132.

Wallin, S. and Johansson, A. V., 2002, "Modelling streamline curvature effects in explicit algebraic Reynolds stress turbulence models", *Journal of Heat and Fluid Flow*, Vol. 23, pp. 721–730.

Wilcox, D. C., 1993, "Turbulence modeling for CFD", DCW Industries Inc.

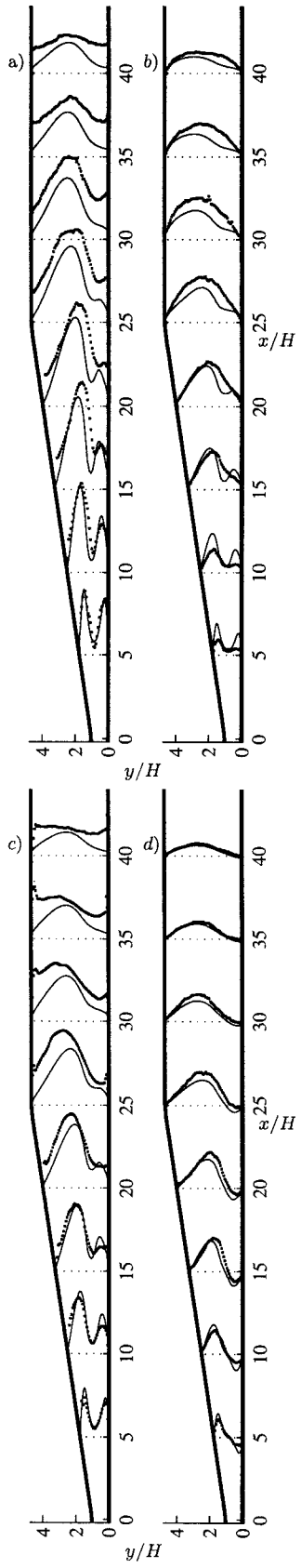

Figure 5: Reynolds shear stresses for the 8.5° case, a) 400 $\overline{u'^2}$, b) 400 $\overline{v'^2}$ c) 400 $\overline{w'^2}$ and d) $\overline{u'v'}$. WJ model (—) and experiments (□)

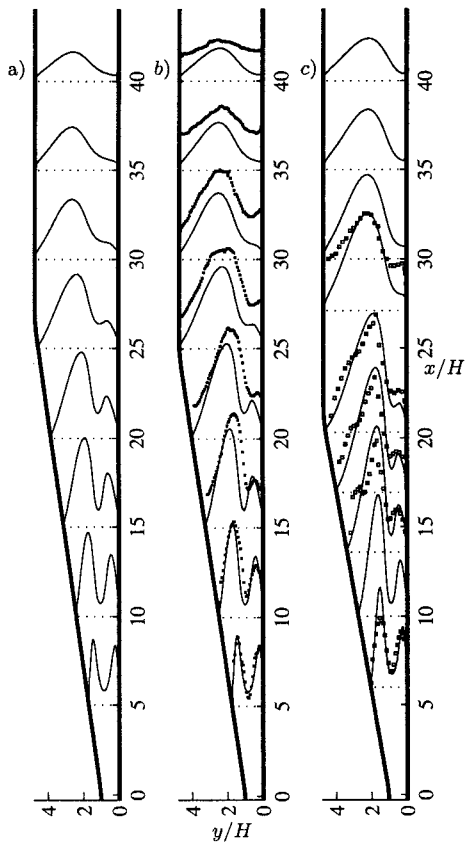

Figure 6: Comparison of Reynolds shear stress 400 $\overline{u'^2}$ for a) 8° case WJ(—), b) 8.5° case WJ(—) and experiments (□) c) 10° case WJ model (—) and experiments (□)

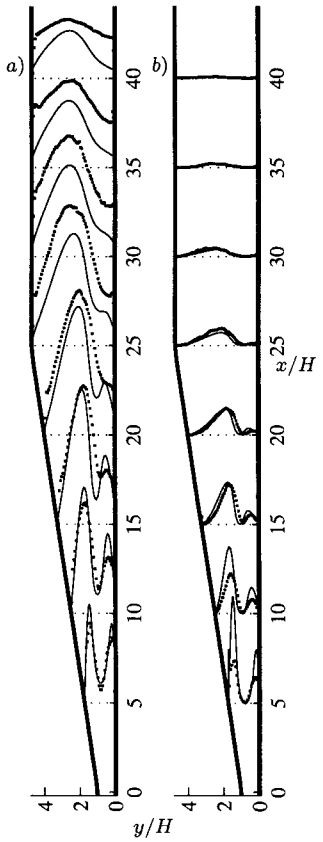

Figure 7: a) Kinetic energy 500 K and b) Production of kinetic energy 1 000 $\mathcal{P}$ in the 8.5° case. WJ (—) and exprinments (□).

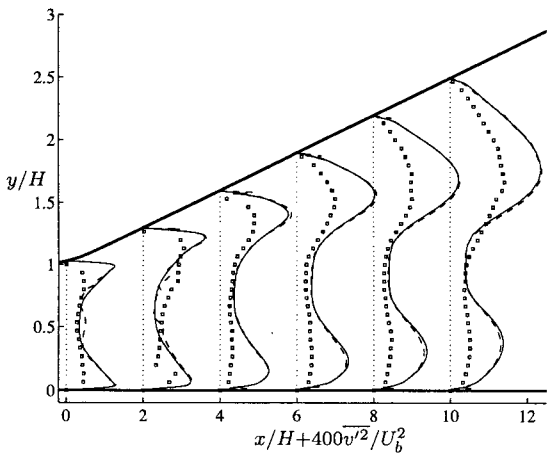

Figure 8: Wall normal Reynolds stress component in the beginning of the 8.5° PAD. Line and symbol notations as in figure 3.

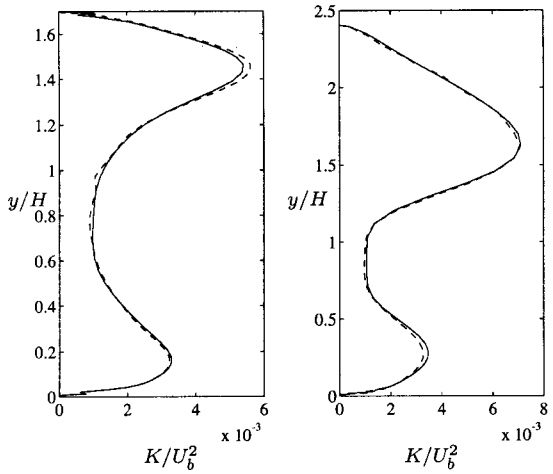

Figure 9: Turbulence kinetic energy at a) $4x/H$ and b) $8x/H$ in the 10° PAD. Solid line denotes WJ and dashed line CC-WJ.